This is a postprint version of the following published document:

Author's Accepted Manuscript

Analysis of the interface and mechanical properties
of field-assisted sintered duplex stainless steels

Andrea García-Junceda, Coral Díaz-Rivera, Víctor
Gómez-Torralba, María Rincón, Mónica Campos,
José Manuel Torralba

**MATERIALS
SCIENCE &
ENGINEERING**

A

Structural Materials: Properties,
Microstructure and Processing

Editor in Chief:
E.J Lavernia

Editors:
E. Werner
M. Starink
J.D. Whittenberger
J.K. Shang

Available online at www.sciencedirect.com
SciVerse ScienceDirect

www.elsevier.com/locate/msea

Cite this article as: Andrea García-Junceda, Coral Díaz-Rivera, Víctor Gómez-Torralba, María Rincón, Mónica Campos and José Manuel Torralba, Analysis of the interface and mechanical properties of field-assisted sintered duplex stainless steels, *Materials Science & Engineering A,* https://doi.org/10.1016/j.msea.2018.10.111
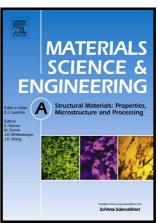
Analysis of the interface and mechanical properties of field-assisted sintered duplex stainless steels.

Andrea García-Junceda[a,*], Coral Díaz-Rivera[b], Víctor Gómez-Torralba[c], María Rincón[b], Mónica Campos[b], José Manuel Torralba[b]

[a] IMDEA Materials Institute, Calle Eric Kandel 2, 28906 Getafe, Madrid, Spain.

[b] Department of Materials Science and Engineering, IAAB, Universidad Carlos III, Av. Universidad 30, 28911 Leganés, Madrid, Spain.

[c] Universidad Rey Juan Carlos, Calle Tulipán s/n, 28933 Móstoles, Madrid, Spain.

[*]Corresponding author at IMDEA Materials Institute, Calle Eric Kandel 2, 28906 Getafe, Madrid, Spain. Tel/Fax numbers: 0034 91 549 34 22/0034 91 550 30 47, andrea.garcia.junceda@imdea.org.
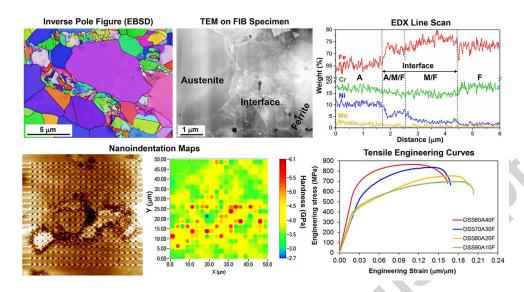
E-mail addresses: andrea.garcia.junceda@imdea.org, 100062132@alumnos.uc3m.es, v.gomezt@alumnos.urjc.es, 100275618@alumnos.uc3m.es, campos@ing.uc3m.es, torralba@ing.uc3m.es

Abstract

The development of duplex stainless steels produced by powder metallurgy represents an interesting alternative to conventional fabrication routes, since typical routes imply a strict control of composition and temperature during the processing path in order to avoid undesirable brittle phases. This work proposes a sintering route, designated as field-assisted hot pressing technique, in which an alternating current is applied to consolidate duplex stainless steels with different initial austenite percentages, always higher than ferrite. In all the cases, a thin and hard planar interface composed by two different microconstituents is generated between austenite and ferrite, growing inside the ferritic phase. The good mechanical properties achieved by these field-assisted sintered duplex stainless steels, in terms of nanohardness, elastic modulus, yield

1

strength, ultimate tensile stress and ductility, establish these steels as promising

candidates to be introduced in the market.

Graphical Abstract.

Keywords: Duplex stainless steel; field-assisted sintering; interface; microstructure;

mechanical properties.

1. Introduction

The industrial interest in duplex stainless steels (DSS) is continually growing. The

attractiveness of these steels is mostly based on the good balance reached between their

mechanical and corrosion properties, as a result of a microstructure mainly formed by

austenite and ferrite phases [1]. The first commercial DSSs were introduced in the

1970s, coinciding with the growth of the oil plants, and many different uses have arisen

since then [2]. They are specially needed in applications in which good mechanical

resistance, together with good toughness and high stress corrosion cracking and pitting

corrosion, are required [3,4].

However, the conventional manufacturing processes present serious drawbacks when

producing DSS. In particular, the need of a rigorous compositional control of alloying

2

elements such as Cr, Ni, Mo and N, and the restriction of the temperature during the whole processing route and shaping treatments, in order to avoid the formation of brittle phases such as sigma-phase, intermetallic phases and different carbides [5-9]. These phases may cause a loss of ductility and decrease the corrosion resistance [7,10-13]. Within this framework, powder metallurgy (PM) emerges as an interesting alternative to avoid the existence of undesirable phases, providing an economic method to process small components with complex shapes and good dimensional tolerances. In addition, PM provides another important advantage, which is the possibility of using different atomized powders as raw materials to tailor the austenite and ferrite contents in the final sintered steel [5]. A considerable number of studies deals with the formation of new constituents between austenite and ferrite, in DSS sintered by PM with austenite contents equal or superior to 50 wt. %, that may affect the mechanical properties [5,13-16]. Ruiz-Prieto *et al.* identified a new constituent in premixes of 430L and 316L steels, which were die pressed under 700 MPa and sintered at 1120 ºC and 1250 ºC during 30 minutes [5]. However, the nature of this interface formed by the diffusion of the main alloying elements has not been clearly explained. The interface has been designed by García *et al*. as a mixed constituent with a plate-like substructure and formed by ferrite, austenite and martensite, which composition is based on the Shaeffler´s diagram [13,17]. In addition, some previous studies have reported that the morphology of the interfacial constituent is similar to that exhibited by the martensitic phase [14], presenting a plate-like shape which thickness varies depending on the composition of the DSS and the sintering process carried out [15]. Attending to Campos *et al.*, this constituent has an acicular shape and may be responsible for the increase of the strength of DSS when a mixture of water and gas atomized powders is used and the sintering takes place in a furnace at 1250 ºC during 180 min under vacuum [18]. On the other

3

hand, Cazzolli described an interface comprising two different constituents, one close to austenite presenting a dual-phase microstructure and another constituent having a plate-like microstructure and close to ferrite [16]. Nevertheless, the effect of this interface on the properties of DSS sintered by field-assisted sintering techniques (FAST) has not been given great attention so far.

The current investigation attempts to analyze the viability of developing new DSS consolidated by field-assisted hot pressing (FAHP) with outstanding mechanical properties. Besides this first objective, the present study explores in more detail the composition and nature of the constituents formed when this technique is applied in a mixture of austenitic and ferritic gas atomized powders with different austenite contents, always superior to 60 wt. %. In consequence, this study is motivated by the need to take into consideration the changes introduced by the use of a FAST technique, which involves shorter diffusion times than conventional sintering methods, on the final microstructure and properties of DSS.

2. Experimental procedure

Duplex stainless steels used in this study are produced from four different mixes of commercial austenitic (316L) and ferritic (430L) gas atomized powders, supplied by Sandvick Osprey Ltd. The chemical composition of the powders and the particle size distribution, determined using a Mastersizer 2000 laser particle size analyzer, are given in Table 1. The morphology of the powders is analyzed by means of scanning electron microscopy (SEM) in an EVO MA15 microscope at an accelerating voltage of 20 kV (Fig. 1). Powder mixtures are prepared in a laboratory turbula mixer and the contents (in wt. %) of AISI 316L/430L are set to 60/40, 70/30, 80/20, 90/10. These mixes are designated as DSS60A40F, DSS70A30F, DSS80A20F and DSS90A10F, respectively.

DSSs are consolidated by FAHP in a Gleeble 3800 apparatus developed by Dynamic System Inc., USA. The powder mixes are poured into a cylindrical graphite die with an internal diameter of 18 mm. This technique implicates the simultaneous application of an uniaxial pressure, by employing two oppositely moving punches to the powders encased in the die, and a low frequency alternating current (AC) favoring the alloying elements diffusion and accelerating the sintering process. In consequence, the powders are heated in a vacuum chamber (10^{-3} Pa) by Joule effect (resistance heating) when the alternating current of 50 Hz is passed into the sample being consolidated through the system anvils. The sintering temperature is set at 1250º C with a heating rate of 100 ºC/min. The samples are maintained at this temperature applying a pressure of 50 MPa during 10 minutes. Subsequently, DSSs are furnace cooled. The temperature is registered during the whole processing route using two K-type thermocouples, one inserted in the graphite punch in which the alternating current is introduced and the other is placed in the center of the die. To avoid the attachment of the steel to the die/punches and to suppress a potential carbon contamination coming from the graphite tools, a high purity tungsten foil (25 μm thick) is used [19]. The consolidated FAHPed-DSSs are cylindrical specimens with 17.95 mm in diameter and 6 mm in length.

The four consolidated DSSs are prepared by standardized techniques for metallographic examination on the longitudinal section with respect to the compression direction of the cylindrical specimen. The relative density is calculated as the average of five measurements by using image analysis on different optical micrographs. To confirm the absence of secondary phases, X-ray diffraction (XRD) patterns are obtained by means of the Cu k_α radiation of an Empyrean PANalytical diffractometer. Moreover, for a deeper characterization of the FAHPed-DSSs a FEG microscope (FEI Helios Nanolab 600i) coupled to electron backscatter diffraction (Oxford Instruments NordlysNano

EBSD detector) is used. The Beraha´s reagent is used to reveal the different microconstituents within the samples [20]. Thus, the quantitative measurement of the constituent's fraction is carried out by point-counting method on at least five SEM micrographs for each DSS [21]. On the other hand, EBSD acquisitions are conducted with an accelerating voltage of 15 kV, a beam current of 5.5 nA and a step size equal to 0.3 μm or 0.04 μm depending on the map magnification. The average austenite grain sizes and the local misorientation maps, evaluating the mean misorientation of a pixel based on the comparison of the orientation of the first layer of neighboring pixels, have been obtained from EBSD acquisitions by using the post-processing software HKL Channel 5.0 supplied by Oxford Instruments, considering grain boundaries with misorientation angles above 5º. The thickness of the interface is calculated from the phase maps, as an average of at least 100 thickness measurements in the regions in which the grains with bcc crystalline structure have small sizes. In addition, FIB samples are obtained to characterize in more detail this interface generated in DSSs with a FEG S/TEM microscope (Talos F200X, FEI) working at 200 kV and equipped with a chemical analysis system via EDX for elemental mapping analysis in different areas. The mechanical properties of the sintered DSSs are assessed by means of nanoindentation and tensile tests. The nanoindentation technique allows to measure the nanohardness (H) and the elastic modulus (E) of different phases existing in DSSs. These data can be determined from the analysis of the load-displacement curves indenting small volumes of material with a diamond tip and using the method developed by Oliver and Pahrr [22]. Nanoindentation tests are carried out on a Hysitron TI950 Triboindenter (Hysitron Inc., Minneapolis, USA) using a Berkovich diamond tip. Hence, in order to target specific grains, square areas are scanned previously to nanoindentation tests, using the scanning probe microscopy (SPM) mode of the

6

nanoindenter instrument. Arrays of 20 x 20 indentations are performed using the high-speed nanoindentation mode of the instrument, with loading, holding and unloading times of 0.3 seconds in total at an imposed maximum force of 5 mN. Spacing between indents is 2.5 µm in both vertical and horizontal directions. Finally, due to the small size of the cylindrical samples obtained, miniature dog-bone tensile samples of 4 mm gauge length and transversal section of 1×1.1 mm^2 are electrodischarge-machined out of the consolidated samples. Tensile tests are carried out at room temperature with a constant crosshead displacement rate equal to 6×10^{-4} mm/s using a screw-driven tensile stage (Kammrath & Weiss, Dortmund, Germany). From the engineering tensile curves, the values of yield strength ($\sigma_{0.2}$), ultimate tensile strength (UTS) and elongation to failure (ϵ) are determined.

3. Results and discussion

3.1 Microstructural characterization

The study of FAHPed-DSSs by SEM microscopy reveals the existence of a heterogeneous biphasic microstructure in which the gray regions represents the ferritic phase, whereas the light gray areas correspond to the majority austenitic phase (Fig. 2). The gray areas corresponding to ferrite are mostly interconnected in DSS60A40F (Fig. 2a). However, the decrease of the ferritic fraction introduced in the mix leads to isolated ferritic islands within an austenitic matrix, as shown in sample DSS90A10F (Fig. 2d). The residual porosity of these PM steels is formed by small and equiaxed pores, mainly located within the austenitic phase since the self-diffusivity of iron in the bcc lattice (ferrite) is approximately two orders of magnitude higher than in the fcc lattice (austenite) [23-25]. Nevertheless, the relative density achieved is always superior to 98.9 %, caused by the large specific surface area exhibited by both gas atomized powders, which is the main driving force for sintering [26]. In addition, it is possible to

distinguish a thin dark gray interface located between ferrite and austenite, which nature will be analyzed in more detail below.

As a first approximation, the identification of the different phases within the sintered stainless steels is analyzed by means of XRD. As shown in the spectra corresponding to the FAHPed-DSSs (Fig. 3), the predominant diffractions come from austenite (fcc) and ferrite (bcc) phases. The presence of a small fraction of martensite (bcc) could be possible in the form of mixed constituents, as will be shown below. However, it is not viable to discriminate martensite among ferrite by XRD since their diffraction peaks would be located at the same angles in the diffractogram. For this reason, some peaks are labeled as Ferrite/Martensite, meaning that a small contribution may be due to the existence of some martensite. Brittle sigma-phase or other undesirable secondary phases such as carbides and/or oxides, hindering both mechanical and corrosion resistances, have not been detected by this technique. Therefore, significant volume fractions of these phases seem to have been eliminated by sintering with FAHP under vacuum atmosphere and using a tungsten foil to avoid the carbon that could diffuse from the graphite matrix and punches.

The measurement of the volume fraction of the constituents by the point-counting method on SEM micrographs as those shown in Fig. 2, demonstrates that the austenite fraction remains unalterable after the consolidation, whereas the ferrite fraction has partially transformed to new interfacial constituents (Table 2). This important finding points towards the growth of the new constituents inside the original ferrite, from austenitic to ferritic particles, and it is consistent with literature in which a decrease of the initial ferrite content introduced in the steel was reported and a mechanism for the formation of an interface at expenses of ferrite was described [14,18].

8

Series of EBSD acquisitions are further conducted on each stainless steel to analyze the microstructure and the interfacial region more exhaustively (Fig. 4). The statistical curves presented in Fig. 5, and obtained from the previous acquisitions, show the austenite grain size distribution in all consolidated samples. These data draw attention to the existence of a restriction in the grain growth of the austenite, caused by the presence of ferrite and interfacial areas randomly dispersed within the matrix. Thus, the average diameter of austenite clearly increases with the decrease of the initial ferritic stainless steel content. In addition, combining the information given by the phase maps (Fig. 4 left) with the values provided by the local misorientation maps (Fig. 4 right), it can be clearly seen that there is an interface surrounding the large equiaxed ferritic grains in which the local deformation is slightly higher (misorientation values around 1-3°) and the grains have smaller size than in the rest of the matrix. Furthermore, after decreasing the step size and increasing the magnification during the map acquisition (Fig. 6), it can be noted that the original austenitic phase is composed by equiaxed grains with a high fraction of Σ3 boundaries, as reported by Haghdadi *et al.* [27]. It is also remarkable that the interface is mainly indexed as a bcc structure also having Σ3 twin faults (<111> type twin) in some regions. Some small and isolated austenite regions are found inside the interface, being preferably located at grain boundaries near a triple junction of ferritic grains, as mentioned by Lischewski and Gottstein for a microalloyed steel in which austenite was nucleated from ferrite [28]. These facts suggest that this interface may be mainly formed by ferrite and twinning martensite, with some small regions of austenite. Moreover, it is possible to observe that the area with local misorientation ranging between 1-3° is also extended some nanometers inside the austenitic constituent with fcc crystal structure (Fig. 6c). Moreover, the inverse pole figure map displayed in Fig. 6d emphasizes that no texture is induced after field-assisted sintering and that the small

9

grains forming the interface have different and random crystalline grain orientations. The average thickness of the interfacial region is measured on phase maps and it can be concluded that it slightly and gradually decreases with the decrease of the ferrite content from 40 % to 10 %, varying from 3.0 μm in DSS60A40F to 1.8 μm in DSS90A10F (being 2.6 and 2.1 μm in samples DSS70A30F and DSS80A20F, respectively). The extension of the interfacial thickness relies on the existence of compositional fluxes leading to an interdiffusion mechanism between particles with different chemical compositions and in direct contact. This generates a gradual Fe and Cr diffusion from ferrite to austenite and Ni and Mo diffusion in the opposite direction (from austenite to ferrite). In order to assess the diffusion profiles in the interfacial area, the concentration variations of the main elements of the alloy (Fe, Cr, Ni and Mo) are deeply analyzed by a STEM-EDX line scan on a FIB-DSS60A40F specimen containing an interface, with a thickness around 2.80 μm, clearly distinguishable (Fig. 7). The line scan is taken from the interior of the austenitic phase and moves along the interfacial region, finally reaching the interior of the ferritic phase. The profiles obtained confirm that the diffusivity of Cr in the Fe lattice at 1250 ºC is higher than the Ni diffusivity, as reported by Oikawa [29], since the distance needed for the Cr to reach a stable composition is shorter for a same sintering time. In addition, due to a low concentration gradient for the Cr existing in the austenite and ferrite phases, this element is more homogeneously distributed within the interfacial area. On the other hand, the diffusivity of Mo in Fe has the highest value and its content is quickly stabilized and approximately null when going across the austenitic grain boundary inside the interface. These STEM-EDX line profiles illustrate a slight depletion of the Cr content in the interface, whereas Fe content is enhanced in the vicinity to the ferritic phase and within approximately one micron and then its concentration starts to decline until reaching the austenite interface. Hence,

10

Ni and Mo diffuse from the austenite to the ferrite constituents decreasing their concentration across the interface, as expected. These variations are clearly displayed in the STEM-EDX maps of Fig. 7, and they suggest that Fe, diffusing from ferrite to austenite, and Ni, moving from austenite to ferrite, are the main elements taking part in the formation of the interfacial constituents due to their high concentration gradients. As an attempt to identify the nature of the constituents formed in the interfacial region, the compositional data obtained from different STEM-EDX area analysis performed in the previous interface are used to calculate the Cr and Ni equivalent and values are introduced in the Schaeffler diagram, as shown in Fig. 8. Although the Schaeffler diagram is principally used for welded structures, it is very useful to illustrate the different areas of stability of stainless steel microstructures in relation to that Cr and Ni equivalent, in wt. % [17]. Thus, by entering the Cr and Ni equivalent values corresponding to the interfacial compositions obtained in the present work for DSS60A40F sample into the Schaeffler diagram of Fig. 8, it is possible to interpret the resulting microstructure. The Schaeffler diagram establishes that there are two new constituents gradually formed, which compositions are evolving on moving from austenite to ferrite. On one side, a mixed constituent with a thickness of around 0.92 μm, formed by austenite, martensite and ferrite (A/M/F constituent) is generated in the region close to the austenitic phase due to a higher Ni content diffusing across the austenite grain boundary. On the other hand, there is a second more extensive mixed constituent, which is adjacent to ferrite and mainly composed by martensite and ferrite (M/F constituent) with a thickness of approximately 1.88 μm. These two mixed constituents with their corresponding thickness are labeled in Fig. 7c to patently show their location in the FIB specimen. To the knowledge of the present authors, only Cazzolli in his doctoral thesis found a wide interface (150-300 μm) comprising two

11

different constituents in a duplex stainless steel sintered at 1300 ºC during 1 h, and using 316L and 430 steel powders [16]. Anyway, his description of this interface and its thickness was quite different from the results presented in this investigation. Cazzolli considered that the interface was evolving from a dual-phase microstructure, formed by ferrite and austenite in the region close to austenite, to a plate-like microstructure composed of ferrite and martensite in the proximity to ferrite. On the other hand, some previous studies have described the interface formed between ferrite and austenite as one unique mixed constituent formed by ternary ferrite-austenite-martensite phases with a chemical composition intermediate between the austenite and ferrite powders [6,15,30]. At this point, it is worth mentioning that Cr has a diffusion distance in the ferritic constituent (bcc), which is an order of magnitude greater than in austenite (fcc) for the same time interval, as reported by Williams and Faulkner [31]. This fact suggests that most of the Cr present in the interface, which has a bcc structure, comes from the ferritic phase. Similar observation can also be made for Fe element diffusing along the interphase, leading to the conclusion that the variations in the thickness values of the complete interfacial region, may be principally caused by the Cr and Fe content available for diffusion mainly coming from the ferritic constituent. Besides, the highest Cr and Fe diffusion rates in the bcc lattice may be the responsible for the formation of the interface at the expense of the original ferrite content introduced in the mix. In the case of DSS60A40F, there exist a larger quantity of ferrite constituent in the mix (40 %). Thus, there are more contacts between ferrite particles and a larger Cr and Fe content diffusing along the ferrite/austenite interface, generating a higher thickness of this interfacial region. Some studies on sintered duplex stainless steels also found that the amount of the mixed A/M/F constituent increased with the original content of ferrite in the mixture [6,15]. Another finding when performing STEM-EDX map analysis, is

12

the identification of some silicon and silicon-manganese oxides, with diameters ranging from 50 up to 200 nm (black phases in the STEM-HADDF image of Fig.7b). Oxides are preferably located at some grain boundaries of the bcc constituents (interface and ferrite). With regard to the analysis of the plastic strain introduced in the material by the creation of this new interfacial region (Fig.9), it is necessary to notice that the boundary between the austenite and the A/M/F constituent is not well defined and a dislocation network, comprising dislocation tangles and tiny loops, has been formed within the austenite (white lines and features in the austenite region of the STEM image in Fig. 9b). Moreover, it is possible to observe some dislocation networks within the interface (Figs. 9a and c). These findings are in accordance with the local misorientation maps previously shown (Figs. 4 and 6), in which the border between austenite and interface was not well defined by a grain boundary and the local strain was greater inside the whole interface and some nanometers within the austenitic phase, probably due to this network of dislocations formed as a consequence of the creation of the interface. Furthermore, the border between M/F and ferritic constituents is well defined by a grain boundary (misorientation angles above 5º) and no dislocation networks are found in the ferritic phase (Figs. 9a and c). These former results may be expected as the higher strength of the ferrite compared to austenite leads to a lower amount of dislocations in the ferritic constituent of duplex steels [32]. This confers the null local misorientation values reached in the ferrite during EBSD acquisitions.

After this microstructural study, it is worth summarizing and highlighting three important findings emerged from the present investigation and related to the interface generated during sintering by FAHP: a) the interface comprises two different mixed constituents: a thin A/M/F constituent in the vicinity of the austenite phase with a boundary not well defined, and a thicker M/F constituent limiting with the ferritic phase

by a grain boundary with misorientation higher than 5º, b) the total thickness of the interfacial area is dependent on the ferrite content (growing with the amount of this phase) and thinner (1.8-3 μm) than the thickness found by other investigations (10-300 μm) in which duplex stainless steels were obtained by conventional routes, following a first uniaxial pressure of the powders and a subsequent furnace sintering [6,14-16], and c) the morphology of the interfacial region tends to be flat, instead of the acicular or plate-like microstructure reported by other authors [5,13-16]. Thus, these facts reveal that the consolidation by FAHP with short sintering times has reduced the time available for the diffusion of the alloying elements, mainly Fe, Cr, Ni and Mo and, consequently, this sintering technique has produced a thin flat interface with two different mixed constituents.

3.2 Mechanical properties

The average values of elastic modulus and hardness obtained from nanoindentation tests at room temperature are displayed in Table 3. In all sintered samples, the ferritic phase possesses higher elastic modulus and hardness values than the austenitic, as may be expected since austenite is softer [33]. However, the main evidence derived from this study indicates that the interfacial mixed constituents exhibit the highest elastic modulus and hardness values in all the sintered FAHPed-DSSs, which is a consequence of three factors acting together in the enhancement of these properties: a) the higher local misorientation values generated in this interface with respect to austenite and ferrite phases (previously shown in the EBSD maps of Figs. 4 and 6), which point to a higher deformation resistance, b) the smaller grain size of the interfacial constituents compared to ferrite and austenite phases, that would enhance the mechanical properties of the steel by the Hall-Petch relationship [34,35], and c) presence of martensite (the strongest and hardest constituent in these DSSs) in both mixed constituents taking part of the

14

interface. On the other hand, it is worth noting that these values reached in the interfacial constituents decrease with the decrease of the ferrite fraction existing in the mixes, providing evidence of the importance on the quantity of Fe and Cr diffusing along the interfacial region in the mechanical response of the material. Thus, results suggest that the higher the global Fe and Cr contents are, due to a higher amount of ferrite content in the mix, the better mechanical properties for both ferritic and interfacial constituents, whereas the properties of austenite are not significantly affected. Fig.10 shows the nanohardness distribution maps obtained for all DSSs sintered in this investigation, together with the corresponding SPM gradient images. The nanoindentation maps visually highlight the existence of some red rims, with high hardness values, corresponding to the interface. The interface (in red) is surrounding the ferritic regions (in yellow). The softer phase, austenite, is mostly shown in green color. These results calculated from nanoindentation tests are consistent with the earlier described microstructural analysis of the different microconstituents forming the FAHPed-DSSs.

Moreover, the effect of the initial austenitic and ferritic stainless steel contents on the mechanical properties can be evaluated observing the stress-engineering strain curves (Fig. 11) measured on miniature specimens for the consolidated DSSs. The values of yield strength, ultimate tensile strength and elongation to failure are determined from these curves and listed in Table 4. Tensile test data show that the strength levels of FAHPed-DSSs improve considerably by increasing the content of the ferritic microconstituent. This fact is due to the particular high tensile strength of ferrite. In addition, the higher ferrite content provides more Fe and Cr diffusing through the interface, generating a greater quantity of mixed constituents in which martensite, with high elastic modulus and hardness values, is always present. When decreasing the ferrite

15

content, the strength is reduced and the ductility improves due to a higher content of soft austenite phase together with a growth of its average grain size. All DSSs exhibit a predominantly ductile behavior and they present a fracture surface mainly composed of spherical dimples formed by microvoid coalescence. Most studies in the literature examined the tensile properties of different DSSs sintered after compaction of austenitic and ferritic stainless steels powder mixes in laboratory furnaces at around 1250 ºC, during periods of time in the range of 30-180 min [5,14, 18,36]. In all these published studies related to DSSs sintered by conventional methods, the tensile values attained for mixes with an approximate content of 50A/50F wt. % were considerably inferior ($\sigma_{0.2}$: 200-220 MPa, UTS: 400-450 MPa and elongation: 0.020-0.025) to the values achieved in the FAHPed-DSSs (Table 4), even for a lower ferritic content, as it is the case of the mixes performed in the present investigation. This improvement in the properties may be probably related to a higher relative densification reached when sintering by a FAST technique and to the avoidance of sigma-phase within the microstructure. Furthermore, from these tests it can be concluded that for the case of DSS60A40F sample, which exhibits the best properties, the obtained tensile values are outstanding since they are similar or even higher than most of the values reported for different commercial annealed DSSs [37]. Apart from the increase of the strength, the field-assisted sintering has improved the kinetic of the sintering process, leading to a thinner hard interface as explained above, which may reduce the embrittlement of the material and seem to have a direct effect in the great enhancement of the ductility.

4. Conclusions

Duplex stainless steels are sintered from different austenitic/ferritic stainless steel powder mixes using a field-assisted technique (FAHP). Important conclusions drawn from this work include:

16

1. The combination of using mixes of gas atomized austenitic and ferritic stainless steel powders and their following sintering by FAHP technique, avoids the presence of brittle and undesirable phases such as sigma-phase, carbides or intermetallic phases. In addition, this solid-state processing technique leads to almost full density DSSs in which a very thin and flat interface is observed between the austenitic and ferritic microconstituents.

2. The microstructural study of the interface reveals that its growth is consuming the original ferritic stainless steel and highlights that it consists of two different mixed constituents predicted by the Schaeffler diagram: a thin microconstituent comprising austenite, martensite and ferrite (A/M/F constituent) generated in the region close to austenite, and a second thicker microconstituent, with a dual phase nature composed by martensite and ferrite (M/F constituent) formed in the region close to ferrite. The formation of these mixed constituents is due to the creation of an interdiffusion mechanism as a response to the existence of different concentration gradient of elements (mainly Fe and Ni) between the austenitic and ferritic stainless steels. The interface exhibits a bcc crystalline structure formed by small grains with local misorientation slightly higher than that presented by ferrite or austenite. Its elastic modulus and its hardness are high due to three different parameters acting together: presence of martensite with high strength and hardness, small grain size, and existence of some local misorientation due to a large quantity of dislocations existing in this region. The interfacial thickness increases with the increase of the original ferritic stainless steel content in the mix since more Fe and Cr content is available for the diffusion.

3. Tensile properties achieved by these FAHPed-DSSs are promising. In particular, the levels of strength and ductility reached by the steel with 40 wt. % of ferrite are higher than the data found in the literature for other DSSs processed by conventional PM

routes, and furthermore, these values are similar or even higher than those published for commercial annealed duplex stainless steels.

Acknowledgements

Data Availability

The raw/processed data required to reproduce these findings cannot be shared at this time as the data also forms part of an ongoing study.

References

[1] K.H. Lo, C.H. Shek, J.K.L. Lai, Recent developments in stainless steels, Mater. Sci. Eng. R 65 (2009) 39-104.

[2] J. Charles, The duplex stainless steels: materials to meet your needs, Duplex Stainless Steels 91 Conference, Beaune, France (1991) 3-48.

[3] J. Charles, 10 years later obviously duplex grades in industrial applications look like a success story, 6th World Duplex Conference and Expo, Venice, Italy (2000) 1-12.

[4] Practical Guidelines for the Fabrication of Duplex Stainless Steels, second ed., Published by the International Molybdenum Association (IMOA), London, UK, 2009.

[5] J. M. Ruiz-Prieto, W. Moriera, J. M. Torralba, L. E. G. Cambronero, Powder metallurgical duplex austenitic-ferritic stainless steels from prealloyed and mixed powders, Powder Metall. 37 (1994) 57-60.

[6] T. Marcu Puscas, A. Molinari, J. Kazior, T. Pieczonka, M. Nykiel, Sintering transformations in mixtures of austenitic and ferritic stainless steel powders, Powder Metall. 44 (2001) 48-52.

[7] V. Muthupandi, P. Bala Srinivasan, S.K. Seshadri, S. Sundaresan, Effect of weld metal chemistry and heat input on the structure and properties of duplex stainless steel welds, Mater. Sci. Eng. A 358 (2003) 9-16.

[8] R. Magnabosco, Kinetics of sigma phase formation in a duplex stainless steel, Mater. Res. 12 (2009) 321-327.

[9] N. Haghdadi, P. Cizek, P.D. Hodgson, V. Tari, G.S. Rohrer, H. Beladi, Effect of ferrite-to-austenite phase transformation path on the interface crystallographic character distributions in a duplex stainless steel, Acta Mater. 145 (2018) 196-209.

[10] C.H Shek, K.W Wong, J.K.L Lai, D.J Li, Hot tensile properties of 25Cr-8Ni duplex stainless steel containing cellular ($\sigma+\gamma2$) structure after various thermal treatments, Mater. Sci. Eng. A 231 (1997) 42-47.

[11]. F. Iacoviello, M. Boniardi, G.M. La Vecchia, Fatigue crack propagation in austeno-ferritic duplex stainless steel 22 Cr 5 Ni, Int. J. Fatigue 21 (1999) 957-963.

[12] C.J. Park, H.S. Kwon, Effects of aging at 475 C on corrosion properties of tungsten-containing duplex stainless steels, Corros. Sci. 44 (2002) 2817-2830.

[13] C. García, F. Martín, Y. Blanco, M.P. de Tiedra, M.L. Aparicio, Corrosion behaviour of duplex stainless steels sintered in nitrogen, Corros. Sci. 51 (2009) 76-86.

[14] M. Campos, A. Bautista, D. Cáceres, J. Abenojar, J.M. Torralba, Study of the interfaces between austenite and ferrite grains in P/M duplex stainless steels, J. Eur. Ceram. Soc. 23 (2003) 2813-2819.

[15] C. García, F. Martín, Y. Blanco, M.L. Aparicio, Effect of ageing heat treatments on the microstructure and intergranular corrosion of powder metallurgy duplex stainless steels, Corros. Sci. 52 (2010) 3725-3737.

[16] M. Cazzolli, PhD Thesis, University of Trento, 2015.

[17] A.L. Schaeffler, Constitution diagram for stainless steel weld metal, Met. Prog. 56 (1949) 680–680B.

[18] M. Campos, J.J. Muñoz, A. Bautista, F. Velasco and J.M. Torralba, Ni diffusion process between austenite and ferrite in a sintered duplex stainless steel obtained by powder mixing, Mater. Sci. Forum 426-432 (2003) 4343-4348.

[19] A. García-Junceda, L. Acebo, J.M. Torralba, Study and suppression of the microstructural anisotropy generated during the consolidation of a carbonyl iron powder by field assisted hot pressing, Metall. Mater. Trans. A 46 (2015) 3192-3198.

[20] G. Petzow, Metallographic Etching, second ed., ASM International, 1999, pp.185.

[21] E.E. Underwood, Quantitative Stereology, Addison-Wesley Publishing Co., Reading MA, 1970, pp. 73-75.

[22] W.C. Oliver, G.M. Pharr, J. Mater. Res. 7 (1992) 1564-1583

[23] F. S. Buffington, K. Hirano, M. Cohen, Self diffusion in iron, Acta Metal. 9 (1961) 434-439.

[24] E. Hämäläinen, A. Laitinen, H. Hänninen, J. Liimatainen, Mechanical properties of powder metallurgy duplex stainless steels, Mater. Sci. Tech. 13 (1997) 103-109.

[25] Shenyan Huang, Daniel L. Worthington, Mark Asta, Vidvuds Ozolins, Gautam Ghosh, Peter K. Liaw, Calculation of impurity diffusivities in α-Fe using first-principles methods, Acta Mater. 58 (2010) 1982-1993.

[26] Andrej Salak: Ferrous powder metallurgy, Cambridge International Science Pub, Cambridge, 1995.

[27] N . Haghdadi, P. Cizek, P.D. Hodgson, V. Tari, G.S. Rohrer, H. Beladi, Effect of ferrite-to-austenite phase transformation path on the interface crystallographic character distributions in a duplex stainless steel, Acta Mater. 145 (2018) 196-209.

[28] I. Lischewski, G. Gottstein, Nucleation and variant selection during the α–γ–α phase transformation in microalloyed steel, Acta Mater. 59 (2011) 1530-1541.

[29] H. Oikawa, Lattice diffusion in iron-a review, Technology Reports of the Tohoku University 48 (1983) 7-77.

[30] P. Datta, G.S. Upadhyaya, Sintered duplex stainless steels from premixes of 316L and 434L powders, Mater. Chem. Phys. 67 (2001) 234-242.

[31] P.I. Williams, R.G. Faulkner, Chemical volume diffusion coefficients for stainless steel corrosion studies, J. Mater. Sci. 22 (1987) 3537-3542.

[32] A. Taisne, B. Décamps, L. Priester, Role of interfaces in duplex stainless steels deformation micromechanisms, Compos. Interface 13 (2006) 89-102.

[33] R. Dakhlaoui, A. Baczmański, C. Braham, S. Wroński, K. Wierzbanowski, E.C. Oliver, Effect of residual stresses on individual phase mechanical properties of austeno-ferritic duplex stainless steel, Acta Mater. 54 (2006) 5027-5039.

[34] E.O. Hall, Proc. Phys. Soc. B 64 (1951) 747-753.

[35] N.J. Petch, J. Iron Steel Inst. 174 (1953) 25-32.

[36] F. Martín, C. García, Y. Blanco, M.L Rodriguez-Mendez, Influence of sinter-cooling rate on the mechanical properties of powder metallurgy austenitic, ferritic and duplex stainless steels sintered in vacuum, Mater. Sci. Eng. A 642 (2015) 360-365.

[37] Metals Handbook, Desk edition, J.R. Davis Ed., second ed., ASM International, Materials Park, Ohio, 1998.

Figure Captions

Fig.1. SE-SEM (SE, Secondary Electron) micrographs of stainless steel powders (a) AISI 316L, (b) AISI 430L.

Fig. 2. BSE-SEM (BSE, Backscatter Electron) images showing the microstructure of FAHPed-DSSs: a) DSS60A40F, b) DSS70A30F, c) DSS80A20F, d) DSS90A10F.

Fig. 3. XRD spectra of the FAHPed-DSSs. γ: Austenite, α/α′: Ferrite/Martensite.

Fig. 4. EBSD observations showing an interface with small grain size, local misorientation between 1-3º and Σ3 twins (white lines). a,c,e,g) Phase maps showing the bcc constituents (ferrite and interface) in red and fcc phase (austenite) in blue for DSS60A40F, DSS70A30F, DSS80A20F and DSS90A10F, respectively. b,d,f,h) Local misorientation maps in the same areas

Fig. 5. Austenite grain diameter distribution and average austenite grain size obtained from EBSD acquisitions in FAPHed-DSSs.

Fig. 6. EBSD for DSS60A40F: a) Phase map showing the bcc constituents (ferrite and interface) in red, fcc phase (austenite) in blue and Σ3 twins in austenite and interface (white lines), b) Local misorientation map in the same area, c) Combination of phase and local misorientation maps, d) Inverse pole figure map.

Fig. 7. (a) BSE-SEM (BSE, Backscatter Electron) micrograph indicating the area selected for the FIB-DSS60A40F specimen preparation, b) STEM-HADDF image showing the selected interfacial line-scan on FIB specimen, c) EDX-line scan profile of the main elements of the steel; STEM-EDX maps for: d) Fe, e) Cr, f) Ni , g) Mo.

Fig. 8. Prediction of the interfacial microstructure using Schaeffler diagram (different STEM-EDX area analysis at the interface of the DSS60A40F are represented as circles). A: Austenite, F: Ferrite, M: Martensite.

Fig. 9. a) Bright field STEM image of dislocation tangles and tiny loops within the FIB-DSS60A40F specimen, b) Austenite-A/M/F border, c) M/F-Ferrite border. The white dotted lines represent the approximate position of the limit between constituents.

Fig. 10. Nanohardness distribution maps on DSSs with their corresponding SPM gradient image: (a) DSS60A40F, (b) DSS70A30F, (c) DSS80A20F, (d) DSS90A10F.

Fig.11. Tensile engineering stress-strain curves of the consolidated DSSs.

List of Tables and Table Captions

Table 1. Chemical composition (in wt. %) and particle size distribution (in μm) of gas atomized stainless steel powders.

Powde	Cr	Ni	Mo	Mn	Si	P	C	S	Nb	Fe	D1	D5	D9
AISI	16.6	10.2	2.1	1.0	0.5	0.0	0.0	0.00	----	Bal	3.5	7.4	15.
AISI	17.2	----	----	0.8	0.8	0.0	0.0	0.01	0.5	Bal	4.8	9.8	20.

Table 2. Ratio of the constituents introduced in the powder mixes (each constituent in wt. %) and after consolidation of DSSs (calculated on SEM images by point-counting method).

Sample	Powder mixes Austenite/Ferrite	FAHPed-DSSs Austenite/(Ferrite&Interfacial Constituents)
DSS60A40F	60/40	(61±4)/(39±4)
DSS70A30F	70/30	(71±2)/(29±2)
DSS80A20F	80/20	(80±2)/(20±2)
DSS90A10F	90/10	(90±1)/(10±1)

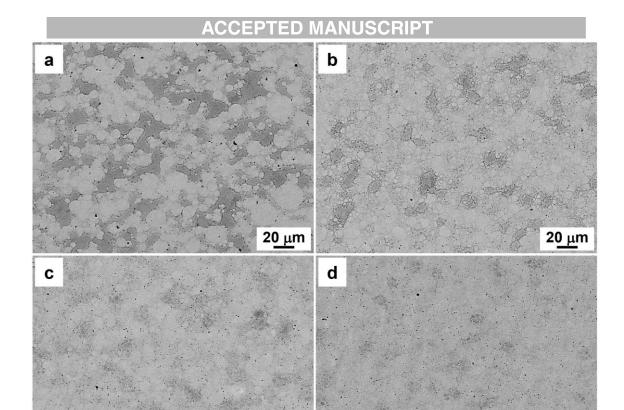**Table 3.** Nanoindentation data of FAHPed-DSSs. (E- Elastic modulus, H-Nanohardness).

	Austenite		Interface		Ferrite	
	E (GPa)	H (GPa)	E (GPa)	H (GPa)	E (GPa)	H (GPa)
DSS60A40F	155 ± 10	3.6 ± 0.2	260 ± 18	6.5 ± 0.3	215 ± 13	4.0 ± 0.3

23

DSS70A30F	150 ± 13	3.5 ± 0.3	253 ± 15	5.7 ± 0.3	211 ± 14	3.9 ± 0.3
DSS80A20F	160 ± 12	3.6 ± 0.4	240 ± 16	5.1 ± 0.4	193 ± 11	3.8 ± 0.4
DSS90A10F	152 ± 11	3.5 ± 0.2	232 ± 20	4.8 ± 0.4	179 ± 12	3.7 ± 0.5

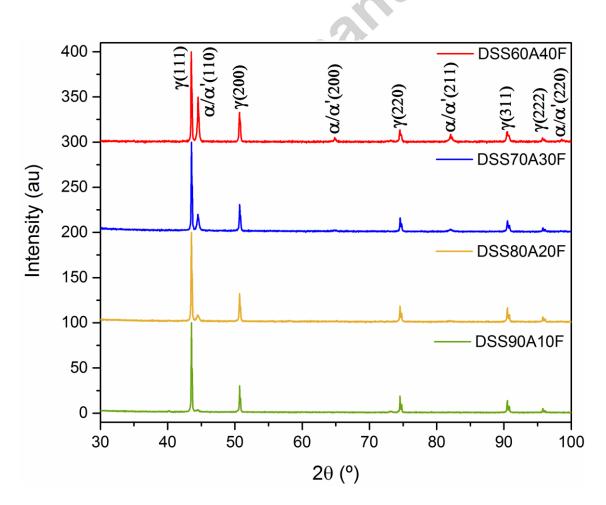**Table 4.** Mechanical properties measured on miniature samples of the studied DSSs.

Sample	$\sigma_{0.2}$ (MPa)	UTS (MPa)	ε
DSS60A40F	592	867	0.165
DSS70A30F	478	839	0.168
DSS80A20F	342	758	0.194
DSS90A10F	349	701	0.205

20 μm

0°   3°